Supplementary Information

Operando X-ray Characterization of High Surface Area Iridium Oxides to Decouple their Activity Losses for the Oxygen Evolution Reaction

Mauro Povia,[1,#] Daniel Abbott,[1,#] Juan Herranz,[1,*] Adrian Heinritz,[1] Dmitry Lebedev,[2] Bae-Jung Kim,[1] Emiliana Fabbri,[1] Alexandra Patru,[1] Joachim Kohlbrecher,[3] Robin Schäublin,[4] Maarten Nachtegaal,[5] Christophe Copéret,[2] and Thomas J. Schmidt[1,6]

[1]Electrochemistry Laboratory, Paul Scherrer Institut, 5232 Villigen, Switzerland

[2]Department of Chemistry and Applied Biosciences, ETH Zurich, Vladimir Prelog Weg. 1-5, CH-8093 Zurich, Switzerland

[3]Laboratory for Neutron Scattering, Paul Scherrer Institute, 5232 Villigen, Switzerland

[4]Scientific Center for Optical and Electron Microscopy, ETH Zurich, Auguste-Piccard-Hof 1, 8093 Zurich, Switzerland

[5]Paul Scherrer Institut, 5232 Villigen, Switzerland

[6]Laboratory of Physical Chemistry, ETH Zurich, 8093 Zurich, Switzerland

# Equal contribution

*Corresponding author: juan.herranz@psi.ch

Experimental information on the *ex situ* characterization techniques

N_2-sorption porosimetry.− The sample IrO_x-AS was characterized by N_2-sorption porosimetry as it was done in our previous paper for a series of IrO_x catalysts that were also synthetized using the modified Adams fusion method.[1] Applying the Brunauer−Emmett−Teller (BET) equation to the data collected with a BELsorp-mini II, the surface area of the IrO_x-AS was determined to be 350 m^2g^{-1}. In the case of the IrO_2-HT catalyst the amount of powder was insufficient to allow a reliable analysis with this technique, and thus its surface area was estimated by interpolation of its double layer capacitance charge in RDE measurements on the capacitance vs. SA plot in Fig. S4c (*vide infra*).

Transmission electron microscopy (TEM).− High resolution TEM images were collected using a TECNAI F30 apparatus operated at 300 kV. Tomography images were collected with a FEI Talos F200X operated in S/TEM mode at 200 kV, tilting the sample holder in and angular range between − 30° and 30° while collecting one image every 40´ of a degree. The specimens were prepared using the as-prepared powders or (for *post-mortem* characterization) parts of the samples that were scratched from the catalytic layers of the flow cell electrodes after 500 degradation potential cycles. The materials were dispersed in a water-isopropanol solution (1:1 in volume) and successively sonicated for 2 min. The resulting solution was drop-casted on a TEM grid (Agar Scientific, holey carbon film - copper, 400 meshes).

X-ray diffraction (XRD).− XRD measurements where performed using a Smartlab Rigaku system equipped with a cupper rotating anode, a graphite Gobel mirror to make the beam parallel and remove the Cu-Kβ radiation, and an SC70 point detector. All measurements were performed in parallel beam mode with the source operating at 200 mA and 45 kV. A slit placed after the Gobel mirror was used to project a beam spot of 2 x 0.3 mm^2 on the samples, which were placed in a Si-zero-background sample holder.

X-ray photoelectron spectroscopy (XPS).− XPS measurements on as prepared and *post-mortem* electrodes of both iridium oxides (i.e., including the Nafion binder) were performed using a VG ESCALAB 220iXL spectrometer (Thermo Fischer Scientific) equipped with an Al Kα monochromatic source (15 kV/150 W,

500 µm beam diameter) and a magnetic lens system. Spectra were collected with a pass energy of 30 eV. The binder's C-F bond in the C 1s spectra at 292.2 eV was used as a reference to correct the binding energies of all acquired spectra.[2] Background subtraction was performed according to Shirley as described in Ref. 3 and the atomic sensitivity factors (ASF) of Scofield were applied to estimate the atomic composition.[4]

The line shape of the Ir 4f lines was determined with a known IrO_2 rutile reference sample (kindly provided by Umicore AG). The Gaussian/Lorentzian product function (GL), Gaussian/Lorentzian sum function (SGL) and the Doniach-Sunjic function (DS) were employed to fit the experimental data and their parameters are reported in the Tables S1-S5 (see values between parentheses). Furthermore, the following constrains were used during the fitting of the XPS data: the separation of the doublet was set to 3 eV, and the satellite main-peak separation to 1.47 eV. The area ratio of the Ir 4f 7/2 to the Ir 4f 5/2 was set to 4:3 and the main-peak to satellite area ratio was set to 4:1. The full widths at half maximum (FWHM) of all Ir 4f and satellite lines, respectively, were constrained to be the same.

Thermogravimetric analysis (TGA).− A TGA measurement of the IrO_x-AS catalyst was performed with a Perkin Elmer TGA 4000 under a continuous O_2 flow of 20 mL·min^{-1}. As shown in Fig. S5a, the temperature protocol consists of an initial temperature hold at 40 °C (green line), followed by a 5 °C·min^{-1} ramp to 100 °C and a 3 h hold to remove moisture in the sample (violet line). Finally, the temperature was further increased from 100 to 900 °C (again, at 5 °C·min^{-1}).

Electrochemical flow cell counterelectrodes' fabrication

An ink consisting of 100 mg of Black Pearls® 2000 carbon (Cabot Corp.), 1 mL of ionomer solution (≈ 5 % Nafion® 117 solution, Sigma Aldrich − leading to an ionomer-to-carbon mass ratio of ≈ 0.4), 6 mL of ultrapure water (18.2 MΩ·cm, ELGA Purelab® Ultra) and 2 mL of isopropanol (99.9% Chromasolv Plus® for HPLC, Sigma Aldrich) was prepared by ultrasonication. Using a mask placed on a hot plate at 100 °C,

this carbon-based ink was spray-coated on two 4 mm diameter areas of a gold-sputtered, pre-cut piece of conductive Kapton foil (DuPont Kapton 200RS100), as to yield a loading of 1.6 $mg_C \cdot cm^{-2}$. Chiefly, these two coated spots are located at the sides of a non-sputtered area of the same diameter that is in terms placed in front of the working electrode upon electrochemical cell assembly (i.e., as to minimize beam absorption by this component). As in the case of IrO_x-based working electrodes, these counter electrodes were weighted using a microbalance (Mettler Toledo XPE206DR) and following the procedures reported in the manuscript (see Eq. 1 for details on how to derive the electrodes' loading).

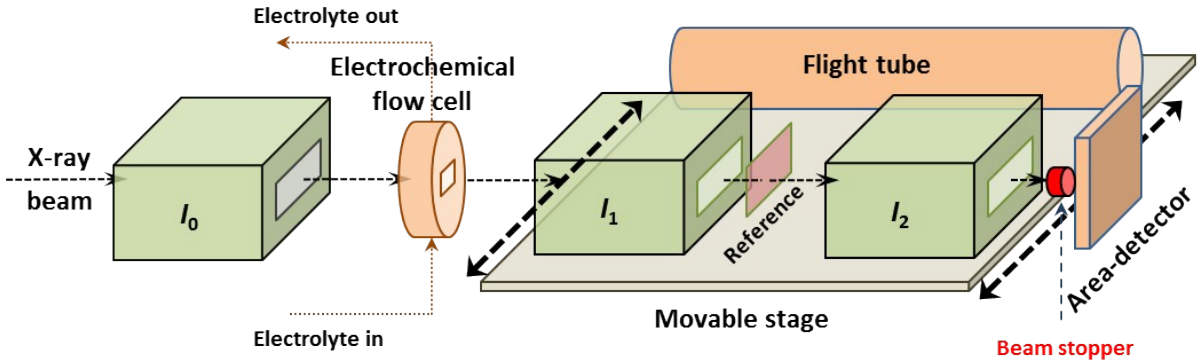

Fig. S1 Scheme of the combined X-ray absorption spectroscopy (XAS) and small angle X-ray scattering (SAXS) set-up. The three green boxes represent the gas ionization detectors for XAS measurements, while the orange plate represents the area detector for SAXS. Following the X-ray beam path from left to right, gas ionization chamber I_0 is always in the same position and measures the intensity of the incoming radiation. A movable stage then hosts the electrochemical flow cell with the analyte, a reference sample (Pt-foil) for XAS energy calibration placed in-between gas ionization chambers I_1 and I_2, and a 580 mm long flight tube. The beam stopper (represented as a small red cylinder) and the area detector are installed on a separate stage and do not move. Note that the stage is moved perpendicular to the beam direction allowing the transition among techniques in ≈ 2 min.

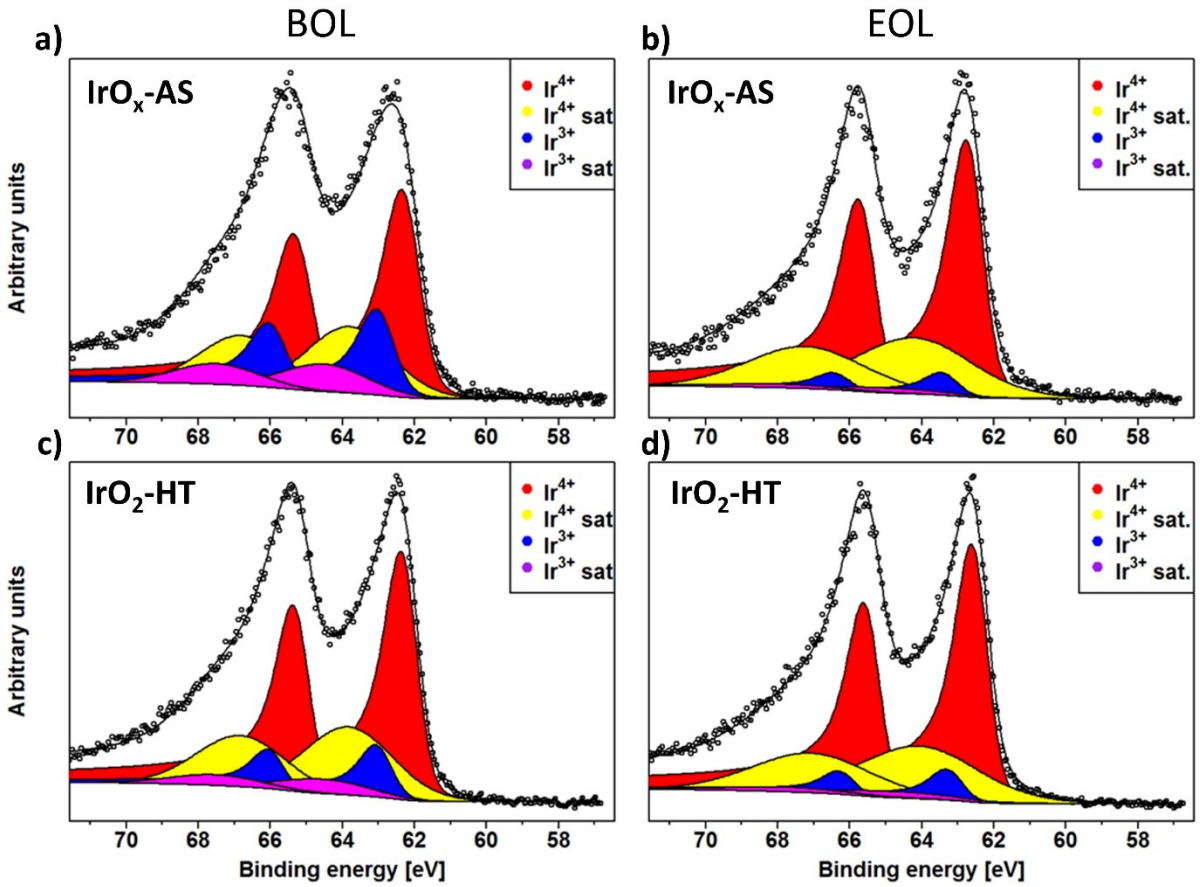

Fig. S2 Deconvoluted X–ray photoelectron spectra recorded on the as-prepared powders processed into electrodes (beginning-of-life, BOL) and on samples removed from the corresponding flow-cell electrodes after the accelerated stress test (end-of-life, EOL). Panels (a) and (b) refer to the IrO_x-AS catalyst (BOL vs. EOL, respectively), while panels (c) and (d) stand for the IrO_2-HT sample (as prepared vs. post-mortem).

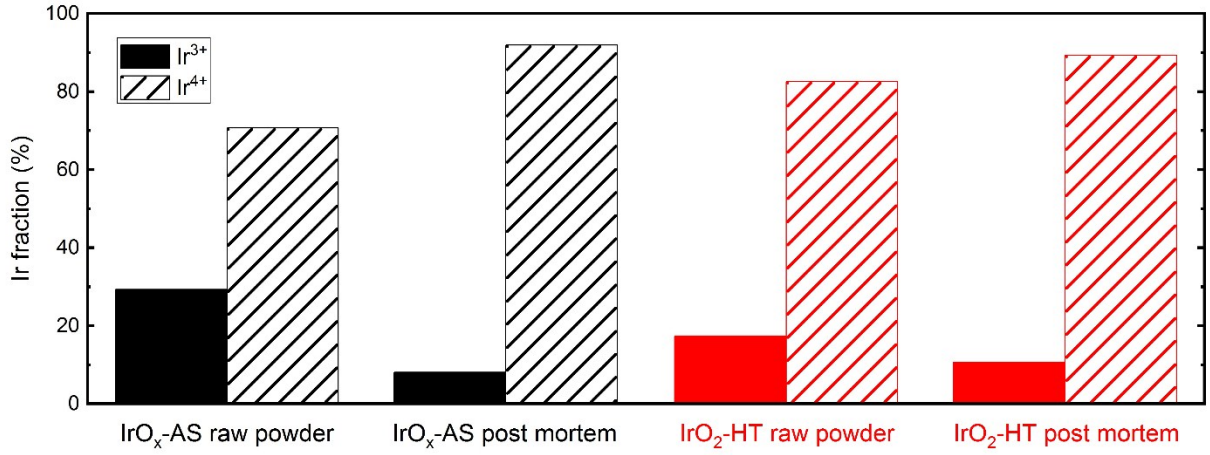

Fig. S3 Surface fraction of iridium in different oxidation states derived from the deconvolution of the XPS results reported in the Figure S2 and summarized in Tables S2 to S5.

Table S1. Summary of the parameters used for the deconvolution of the rutile IrO_2 reference sample used as a basis for XPS data deconvolution, whereby the line shapes correspond to a Gaussian/Lorentzian product function (GL), Gaussian/Lorentzian sum function (SGL) or a Doniach-Sunjic function (DS), respectively.

Component	Line shape	FWHM (eV)(eV)		Binding energy (eV)	
		4f7/2	4f5/2	4f7/2	4f5/2
Ir^{4+}	DS(0.2,230), SGL(20)	1.08	1.08	62.08	65.08
Ir^{4+} satellite	GL(20)	3.23	3.23	63.55	66.55

Table S2. Summary of the XPS deconvolution results for the IrO_x-AS electrode (i.e., including Nafion binder), for which the deconvoluted spectrum appears plotted in Fig. S2a. Note that the line shapes correspond to a Gaussian/Lorentzian product function (GL), Gaussian/Lorentzian sum function (SGL) or a Doniach-Sunjic function (DS), respectively.

Component	Line shape	FWHM (eV)		Binding energy (eV)		At. Ratio (at. %)
		4f7/2	4f5/2	4f7/2	4f5/2	
Ir^{4+}	DS(0.2,230)SGL(40)	1.16	1.16	62.34	65.34	70.7
Ir^{4+} satellite	GL(20)	2.78	2.78	63.81	66.81	
Ir^{3+}	DS(0.2,230)SGL(40)	1.16	1.16	63.04	66.04	29.3
Ir^{3+} satellite	GL(20)	2.93	2.93	64.51	67.51	

Table S3. Summary of the XPS deconvolution results for the IrO_x-AS sample at the end of the accelerated stress test, for which the deconvoluted spectrum appears plotted in Fig. S2b. Note that the line shapes correspond to a Gaussian/Lorentzian product function (GL), Gaussian/Lorentzian sum function (SGL) or a Doniach-Sunjic function (DS), respectively.

Component	Line shape	FWHM (eV)		Binding energy (eV)		At. Ratio (at. %)
		4f7/2	4f5/2	4f7/2	4f5/2	
Ir^{4+}	DS(0.2,230)SGL(40)	1.10	1.10	62.76	65.76	91.9
Ir^{4+}sat.	GL(20)	3.86	3.86	64.23	67.23	
Ir^{3+}	DS(0.2,230)SGL(40)	1.10	1.10	63.46	66.46	8.1
Ir^{3+} sat.	GL(20)	3.86	3.86	64.93	67.93	

Table S4. Summary of the XPS deconvolution results for the IrO_2-HT electrode (i.e., including Nafion binder), for which the deconvoluted spectrum appears plotted in Fig. S2c. Note that the line shapes correspond to a Gaussian/Lorentzian product function (GL), Gaussian/Lorentzian sum function (SGL) or a Doniach-Sunjic function (DS), respectively.

Component	Line shape	FWHM (eV)		Binding energy (eV)		At. Ratio (at. %)
		4f7/2	4f5/2	4f7/2	4f5/2	
Ir (IV)	DS(0.2,230)SGL(40)	1.05	1.05	62.37	65.37	82.6
Ir (IV) sat.	GL(20)	2.93	2.93	63.84	66.84	
Ir (III)	DS(0.2,230)SGL(40)	1.05	1.05	63.04	66.04	17.4
Ir (III) sat.	GL(20)	2.93	2.93	64.54	67.54	

Table S5. Summary of the XPS deconvolution results for the IrO_2-HT sample at the end of the accelerated stress test, for which the deconvoluted spectrum appears plotted in Fig. S2d. Note that the line shapes correspond to a Gaussian/Lorentzian product function (GL), Gaussian/Lorentzian sum function (SGL) or a Doniach-Sunjic function (DS), respectively.

Component	Line shape	FWHM (eV)		Binding energy eV		At. Ratio (at. %)
		4f7/2	4f5/2	4f7/2	4f5/2	
Ir^{4+}	DS(0.2,230)SGL(40)	1.04	1.04	62.61	65.61	89.3
Ir^{4+} sat.	GL(20)	3.91	3.91	64.08	67.08	
Ir^{3+}	DS(0.2,230)SGL(40)	1.04	1.04	63.31	66.31	10.7
Ir^{3+} sat.	GL(20)	3.91	3.91	64.78	67.78	

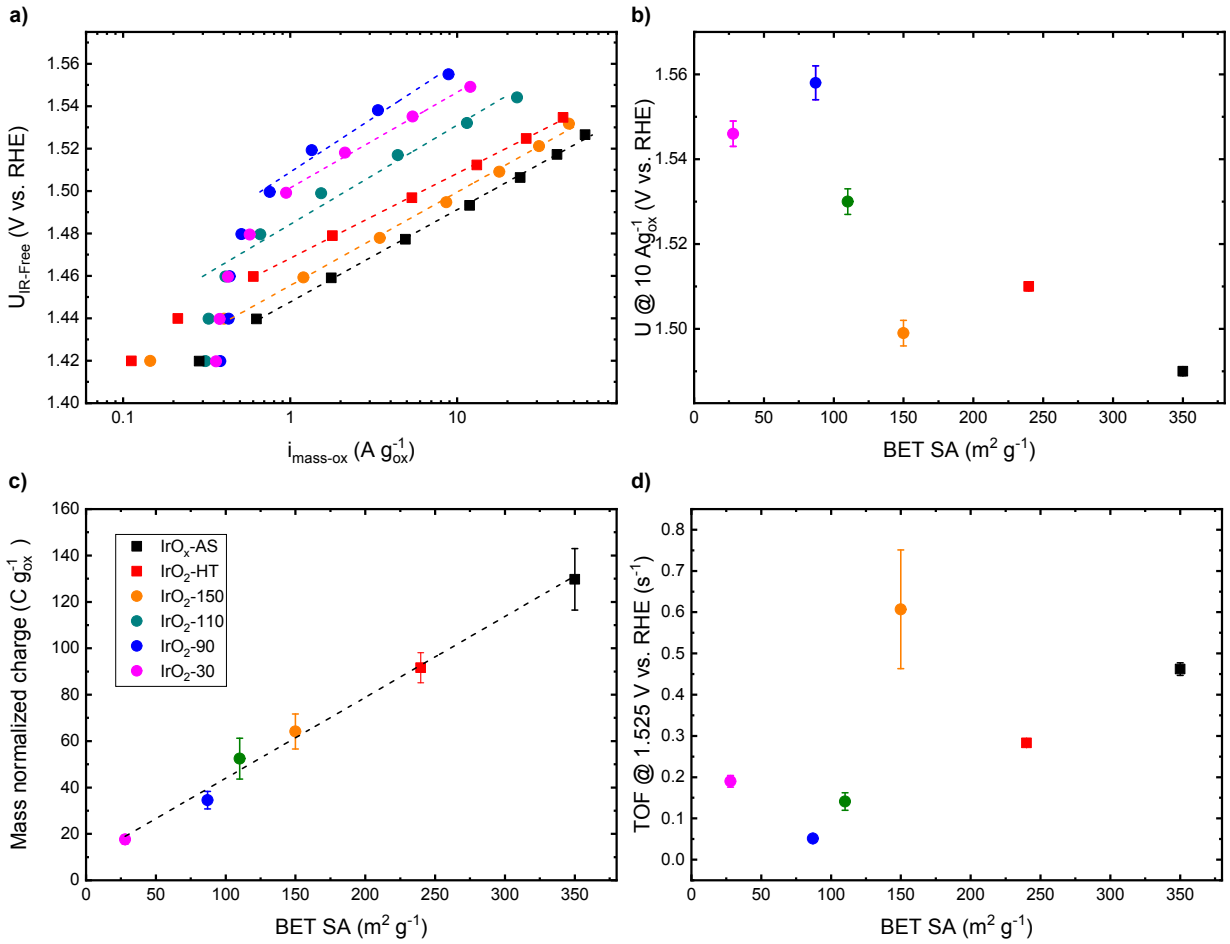

Fig. S4 Comparison of the BOL electrochemical behavior displayed by the iridium oxides in Ref. 1 (represented as circles) and the IrO_x-AS and IrO_2-HT samples included in this study (square symbols). Mass-normalized Tafel plots (a); relation between the catalysts' surface area (SA, derived from the N_2-sorption results) and the potential at an OER-current of 10 $A \cdot g_{oxide}^{-1}$ (b), the capacitive charge between 1.0 and 1.4 V vs. RHE (c) and the turnover frequency (TOF) at 1.525 V vs. RHE. Note that the SA of the IrO_2-HT sample was estimated by interpolation of its capacitive charge into the linear trend in panel (c).

Table S6. Summary of the surface area (SA) values and electrochemical parameters displayed in Figure S4.

Sample	Surface area ($m^2 \cdot g^{-1}$)	Tafel slope ($mV \cdot dec^{-1}$)	U@ 10 Ag_{ox}^{-1} (V vs. RHE)	i_m@ 1.525 V vs. RHE ($A \cdot g_{ox}^{-1}$)	TOF (s^{-1})
IrO_x-AS	350	43.4±0.4	1.490±0.001	55.4±3.0	0.462±0.015
IrO_2-HT	250	40.4±0.7	1.509±0.001	26.0±0.4	0.283±0.002
IrO_2-150	150	43.9±2.4	1.499±0.003	37.0±7.9	0.610±0.140
IrO_2-110	110	38.3±1.3	1.530±0.003	7.3±1.1	0.141±0.021
IrO_2-90	87	43.7±2.3	1.558±0.004	1.8±0.2	0.051±0.002
IrO_2-30	28	44.9±1.9	1.546±0.003	3.3±0.4	0.190±0.014

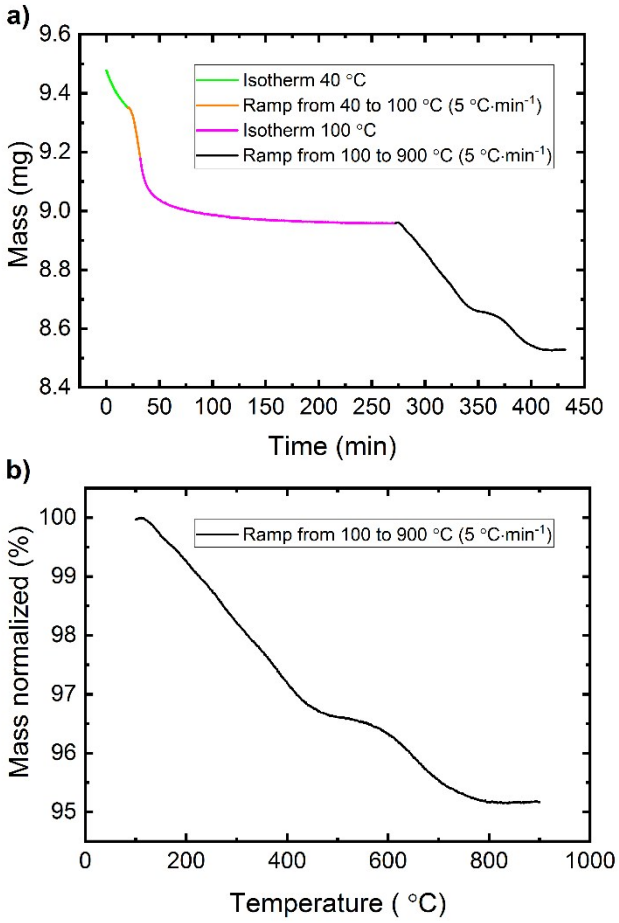

Fig. S5 Time-dependent mass loss undergone by the IrO_x-AS catalyst in the course of the TGA measurement under a continuous O_2-flow of 20 $mL \cdot min^{-1}$, consisting of an initial hold at 40 °C (green line) followed by a 5 $°C \cdot min^{-1}$ ramp to 100 °C, a 3 hour hold at this temperature, and a second ramp (at the same rate) up to 900 °C (a). Normalized mass loss undergone by the sample during the heating ramp from 100 to 900 °C (b).

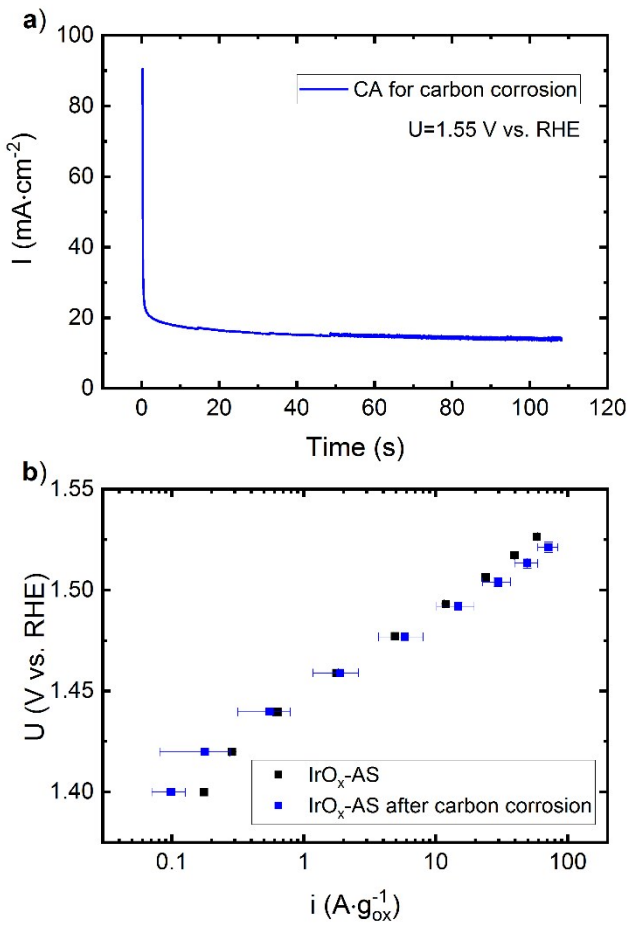

Fig. S6 Example of the time vs. current response recorded in the chronoamperometric treatment step performed to oxidize the carbon layer atop the IrO_x-AS catalyst surface (a), whereby a rotating disc electrode loaded with ≈ 100 $\mu g_{catalyst} \cdot cm^{-2}$ was submitted to a chronoamperometric step at 1.55 V vs. RHE until a charge of 1700 $mC \cdot cm^{-2}$ was attained. Compared polarization curves recorded on the as-prepared IrO_x-AS catalyst (black squares) or the same catalyst having undergone the chronoamperometric step described above (blue squares − b); note that error bars represent standard deviations averaged for three independent measurements.

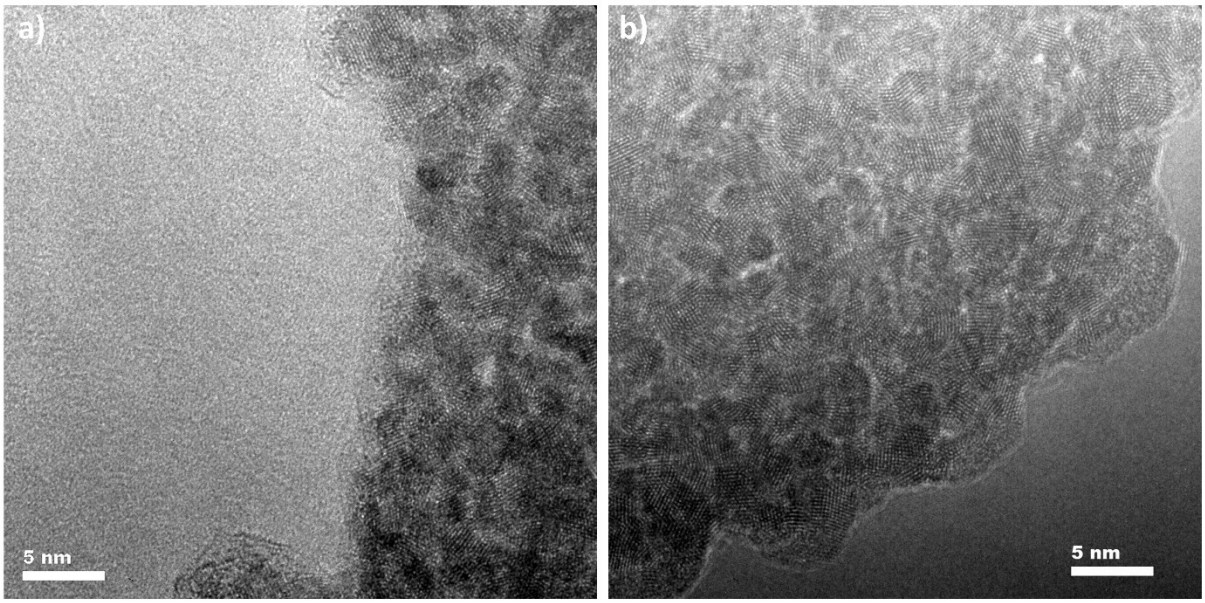

Fig. S7 Transmission electron micrographs of the IrO_x-AS catalyst processed in the form of an ink for RDE measurements (a) or after having undergone a chronoamperometric step at 1.55 V vs. RHE until a charge of 1700 $mC \cdot cm^{-2}$ was attained. Note the presence of a ≈ 2 nm thick carbon layer atop the catalyst in (a), along with the absence of the latter C-deposit in the CA-treated sample displayed in (b).

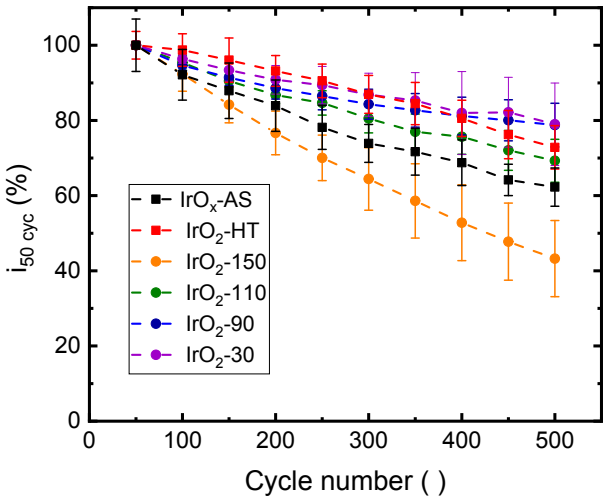

Fig. S8 Compared stability of the different IrO_2-catalysts included in Ref. 1 (circle symbols) and the IrO_x-AS and IrO_2-HT samples in this study (square symbols), expressed as the OER-current at 1.6 V vs. RHE, normalized with respect to the value measured in the 50th degradation cycles.

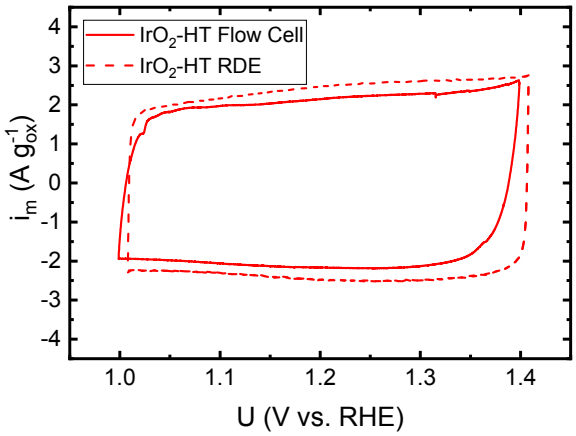

Fig. S9 Comparison of the mass-normalized cyclic voltammograms recorded on the IrO_2-HT catalyst in flow cell vs. RDE configurations (10 $mV \cdot s^{-1}$, air-saturated 0.1 M $HClO_4$), whereby the catalyst loadings were ≈ 100 vs. ≈ 5,400 $\mu g \cdot cm_{IrOx}^{-2}$ for RDE vs. flow cell tests, respectively.

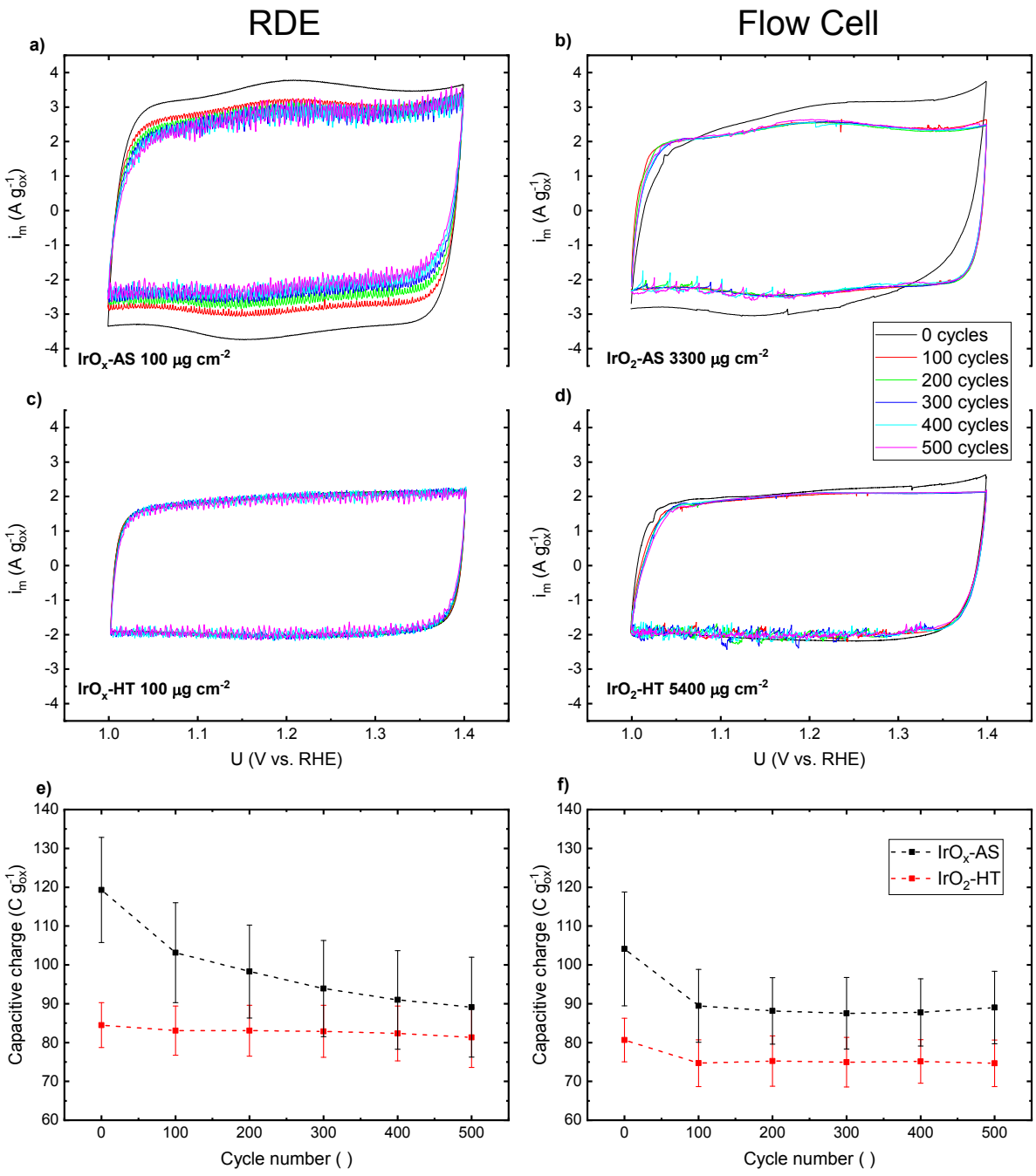

Fig. S10 Cycle-dependent, mass-normalized cyclic voltammograms (10 mV·s^{-1}, air-saturated 0.1 M $HClO_4$) recorded in RDE vs. flow cell configurations (panels a and c vs. b and d, respectively) for both catalysts, implementing the corresponding loadings specified in each panel. The corresponding cycle-dependent, mass-normalized capacitive charges (averaged for three independent measurements on different electrodes) recorded in RDE vs. flow cell are displayed in panels e vs. f, respectively.

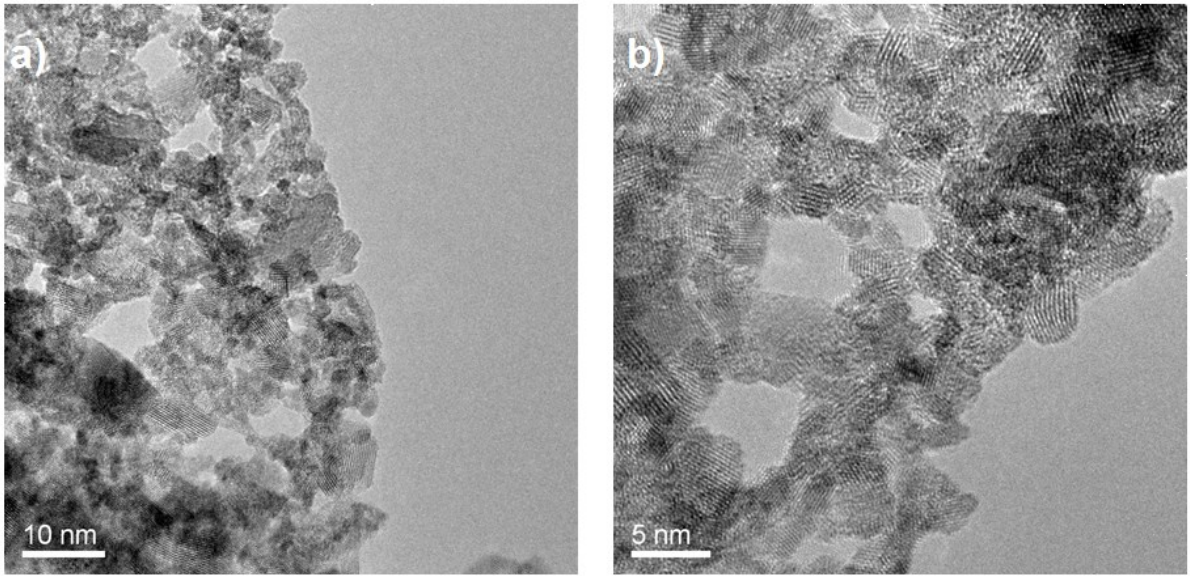

Fig. S11 HR-TEM images of the as-prepared IrO_2-HT catalyst.

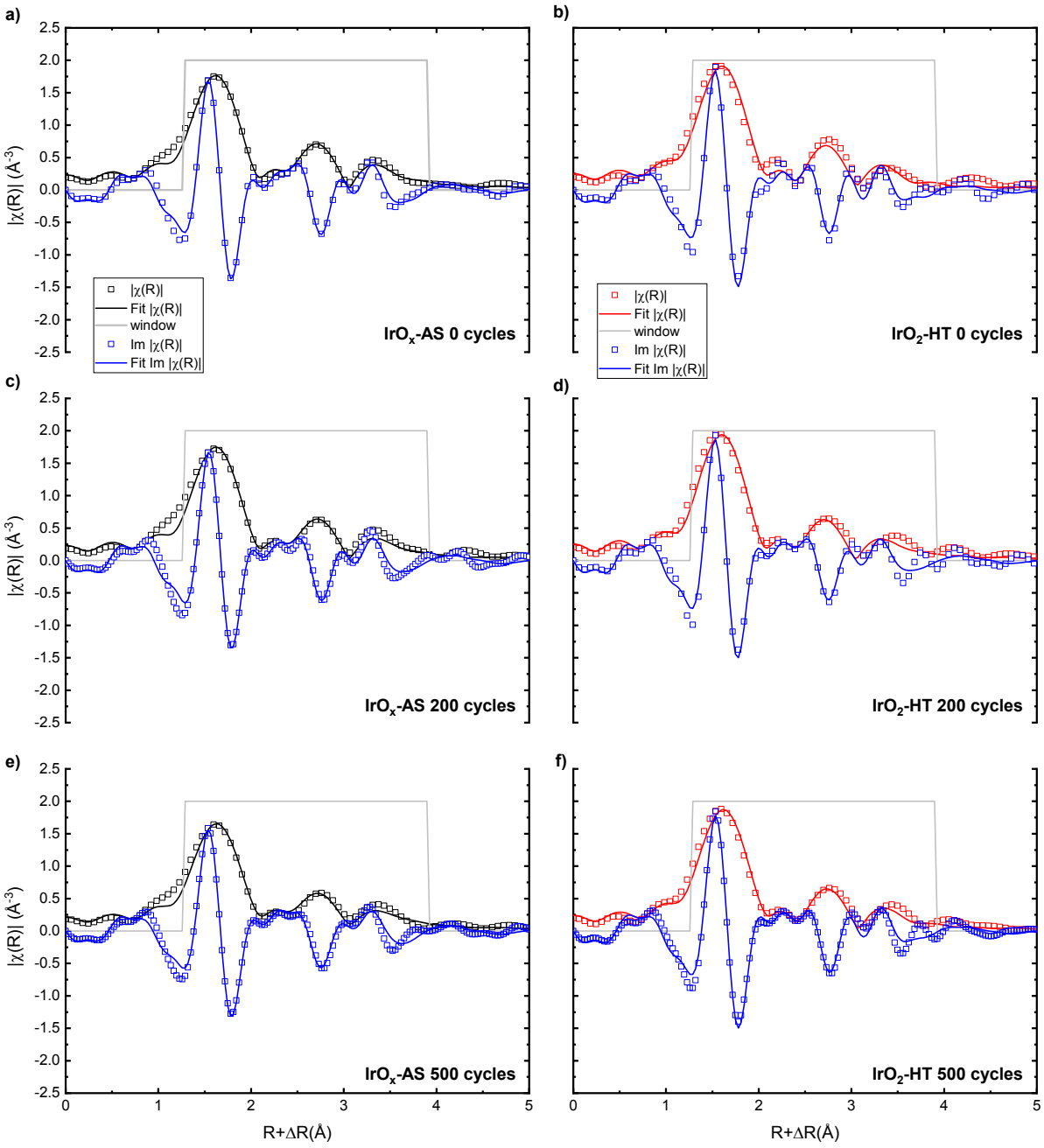

Fig. S12 Cycle-dependent, Fourier-transformed EXAFS and corresponding fits (square points vs. solid lines, respectively) acquired *in situ* while holding the potential at 1.0 V vs. RHE for IrO_x-AS (panels a, c and e) or IrO_2-HT (panels b, d and f).

Table S7. Summary of the parameters derived from the fitting of the cycle-dependent, Fourier-transformed EXAFS of the IrO_x-AS sample displayed in Fig. S12, whereby NN refers to the number of nearest neighbors, E_0 is the energy shift, R refer to the bond scattering distances for the 1st and 2nd shells (i.e., Ir-O vs. Ir-Ir bonding distances), σ^2 is the Debye-Waller factor, and the R-factor is a statistic parameter for which values below 0.02 are regarded as indicative of a good quality EXAFS fit.[5]

Sample	Scattering path	NN	E_0 (eV)	R (Å)	σ^2 (Å^2)	R-factor
IrO_x-AS, 0 cycles	Ir-O	6.4±0.8	13.0±0.8	2.015±0.009	0.003±0.002	0.012
	Ir-Ir	19.6±6.1		3.140±0.018	0.016±0.004	
IrO_x-AS, 200 cycles	Ir-O	6.2±1.0	13.0±1.1	2.018±0.011	0.003±0.002	0.021
	Ir-Ir	17.4±7.8		3.149±0.026	0.016±0.006	
IrO_x-AS 500, cycles	Ir-O	6.3±1.1	13.8±1.1	2.020±0.012	0.004±0.002	0.022
	Ir-Ir	19.5±9.3		3.151±0.031	0.020±0.008	

Table S8. Summary of the parameters derived from the fitting of the cycle-dependent, Fourier-transformed EXAFS of the IrO_2-HT sample displayed in Fig. S12, whereby NN refers to the number of nearest neighbors, E_0 is the energy shift, R refer to the bond scattering distances for the 1st and 2nd shells (i.e., Ir-O vs. Ir-Ir bonding distances), σ^2 is the Debye-Waller factor, and the R-factor is a statistic parameter for which values below 0.02 are regarded as indicative of a good quality EXAFS fit.[5]

Sample	Scattering path	NN	E_0 (eV)	R (Å)	σ^2 (Å^2)	R-factor
IrO_2-HT, 0 cycles	Ir-O	6.9±1.4	12.6±1.6	2.001±0.015	0.004±0.003	0.035
	Ir-Ir	11.2±7.5		3.144±0.029	0.010±0.007	
IrO_2-HT, 200 cycles	Ir-O	6.4±1.2	12.6±1.5	1.998±0.013	0.002±0.003	0.032
	Ir-Ir	14.2±9.0		3.139±0.033	0.015±0.008	
IrO_2-HT, 500 cycles	Ir-O	6.7±1.2	13.4±1.4	2.011±0.013	0.003±0.003	0.027
	Ir-Ir	11.6±6.8		3.157±0.027	0.011±0.006	

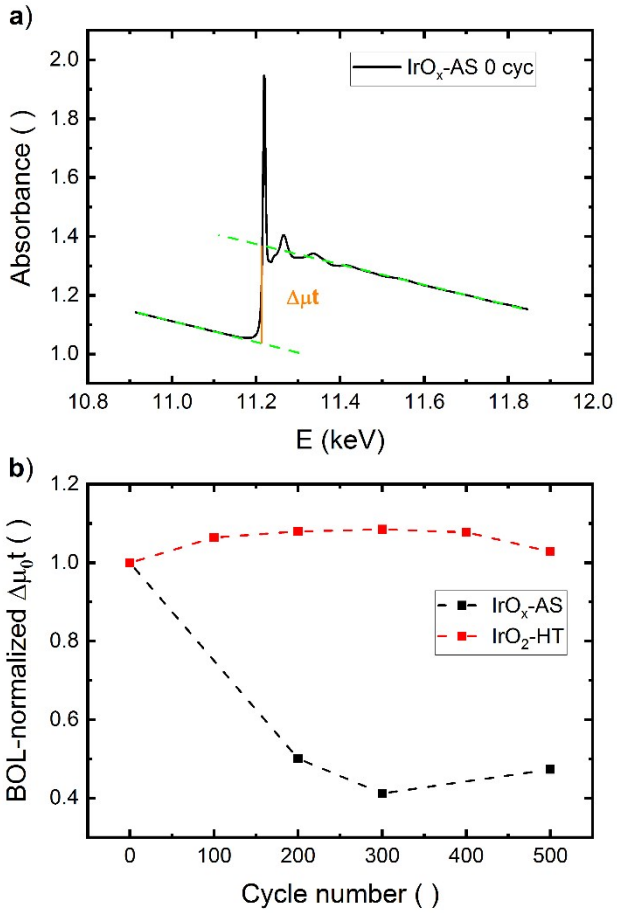

Fig. S13 *In situ*, non-normalized XAS spectrum acquired at BOL for the sample IrO_x-AS (a), illustrating the absorption height denoted Δμt. Corresponding, cycle-dependent Δμt-values normalized with respect to this BOL magnitude (b).

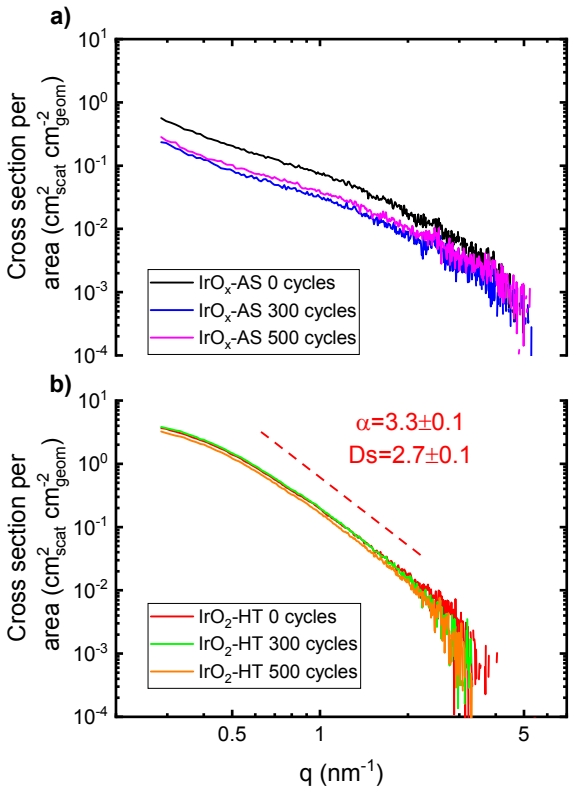

Fig. S14 Cycle-dependent, *in situ* A-SAXS curves recorded at 1.0 V vs. RHE in the course of the accelerated stress test for the IrO_x-AS (a) and IrO_2-HT (b) samples. Note that the value of α in (b) refers to the slope of the dashed straight line in the same panel.

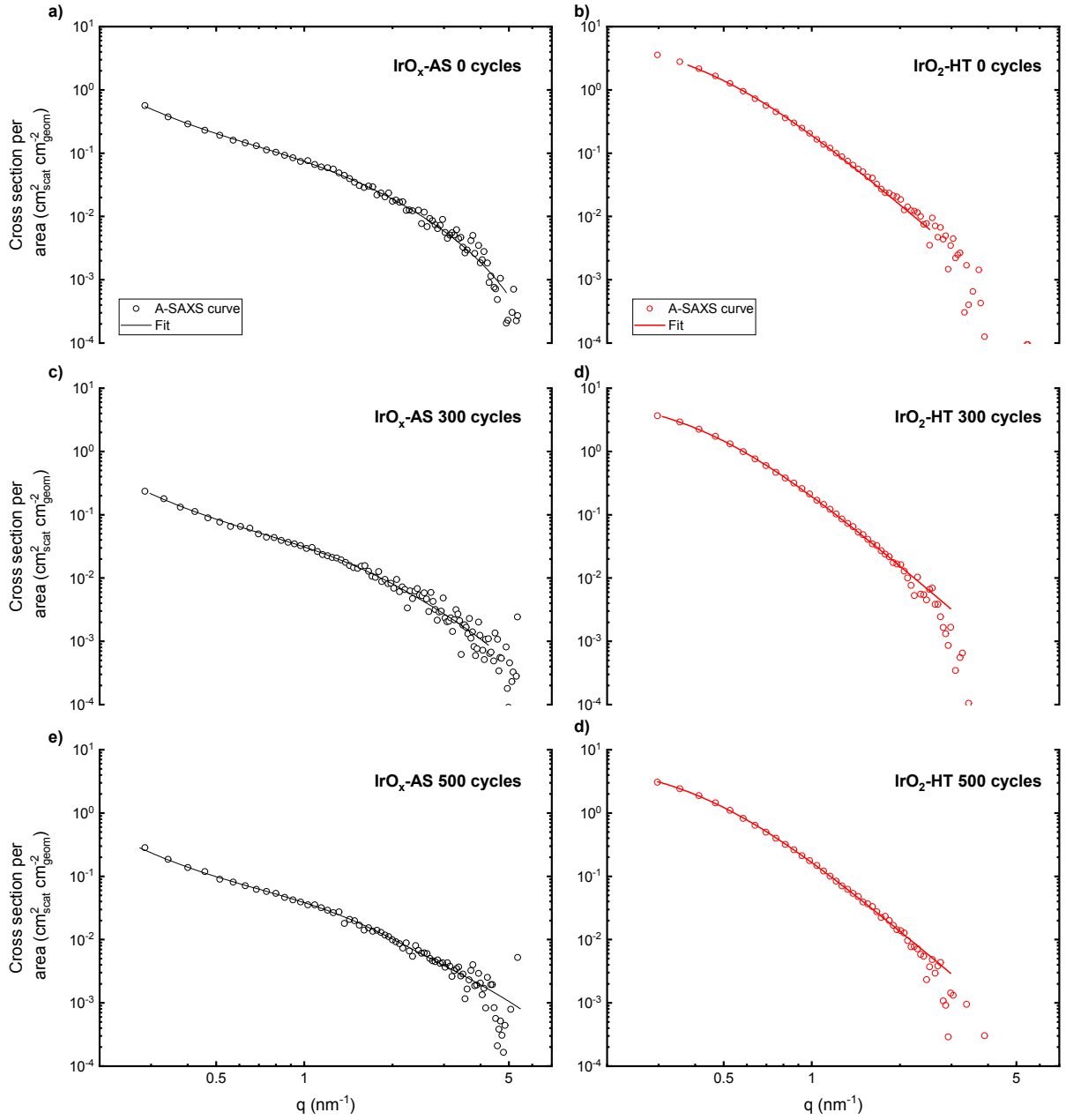

Fig. S15 Fits of the cycle dependent, *in situ* A-SAXS curves (recorded at 1.0 V vs. RHE) presented in Fig. S14 that were completed assuming a cylindrical particle shape for IrO_x-AS or using the generalized Debye-Anderson-Brumberger model for IrO_2-HT. Note that empty circles represent the experimental data, while solid lines correspond to their fits.

Fundamentals of the models applied for A-SAXS data analysis

A-SAXS curves data collection.− All data were collected at a potential of 1.0 V *vs.* RHE and processed according the procedures reported in our previous work.[6] Following normalization of the experimental data, the A-SAXS curves are reported in Figs. S14 and S15 as cross section per area vs. $\left(\frac{1}{A}\frac{d\sigma}{d\Omega}\right)_{IrOx}$ vs. the module of the scattering vector (q), defined as follows:

$$q = \frac{4\pi}{\lambda} sin\theta \qquad [S1]$$

where λ is the wave length of the monochromatic X-ray beam used for the measurement, and 2θ is the scattering angle. In Fig. S15, the circular points correspond to the experimental data, while the solid lines are the fitting curves.

Fitting model of the IrO_x-AS sample's A-SAXS curves.− The cycle-dependent, *in situ* scattering curves of the IrO_x-AS catalyst were fitted applying a model that consists of a form factor $P(q)$ and a structure factor $S(q)$, whereby $P(q)$ is a flat disk and $S(q)$ is a Gaussian mass fractal. Specifically, the particles in IrO_x-AS can be described as disks of diameter (D) larger than their thickness (L), and the fitting model calculates the lognormal distribution of the diameter and an average thickness value, $<L>$.

The structure factor is the Fourier transform of the density auto correlation function, $g(\mathrm{R})$, which represents the area where the cluster electron density is constant:[7]

$$\mathrm{S}(q) = \int \mathrm{e}^{\mathrm{i}\vec{q}R} g(\mathrm{R}) dR \qquad [S2]$$

Additionally, for a fractal system:[8]

$$\mathrm{g}(R) = \frac{D_f}{4\pi R_0^{D_f}} R^{D_f - d} h\left(\frac{R}{\xi}\right) \qquad [S3]$$

where R is a variable related to the cluster size, d is the Euclidean spatial dimension (which is equal to 3, since the fractal is placed in a three-dimensional space), and R_0 is the characteristic size of each individual unit forming the cluster. Finally, the last term of Eq. S3 ($h(R/\xi)$) is the so-called cutoff function, which for most fractals follows the expression:[8]

$$h\left(\frac{R}{\xi}\right) = e^{-\left(\frac{R}{\xi}\right)^{\beta}} \qquad [S4]$$

where β is an exponent related to the fractal characteristic and ξ is the correlation length whereby the electron density is constant. From a mathematical point of view, the value of the cutoff function drops drastically to zero when R > ξ, at which point also $g(R)$ becomes zero, so that the electron density is zero out of the fractal.

As reported in our previous work, the data were initially analyzed including β as a fitting parameter.[6] Since the value of β derived from these initial fits was systematically ≈ 2, the fits were repeated imposing β=2, which led to a better estimation of the error. Since the exponent of the cutoff function is β=2, Equation S4 becomes similar to the Gauss function, and thus the structure function $S(q)$ is referred to as a Gaussian mass fractal. Sorensen and Wang reported the relation between ξ and the gyration radius (Rg, i.e., the characteristic size of the cluster formed by agglomerated particles) for different kinds of cutoff functions. In the specific case of the Gaussian cutoff, these variables are correlated as follow:[7]

$$\xi^2 = \frac{4}{D_f} R_g^2 \qquad [S5]$$

The mass fractal dimension D_f was fitted following an approach similar to that used to estimate β. In a first approximation, D_f was a fitting parameter that was systematically estimated to have a value of ≈ 2, at which point the condition $D_f = 2$ was imposed for all subsequent fits. This result also indicates that the particles agglomerate bi-dimensionally (*vide infra*).

Finally, having estimated D_f and R_g, these variables can be combined to derive the average number of particles in each fractal agglomerate, <N>:[7]

$$< N >= \left(\frac{R_g}{R_0}\right)^{D_f} \quad [S6]$$

where R_0 is the characteristic size of the particle. Since the flat disk model used to fit the A-SAXS curves implies that the disks feature a diameter larger than their thickness (i.e., $D > L$), D can be regarded as these disks' representative dimension. Therefore, the calculation was performed assuming that R_0 in Eq. S6 is equal to the disk's average radius (<R>, in terms calculated by dividing by two the average diameter (<D>) derived from the fit's log normal distribution, i.e., <R>=<D>/2). The cycle-dependent changes of <N> and R_g in the course of the AST appear plotted in Fig. S19.

Fitting model of the IrO_2-HT sample's A-SAXS curves.− The A-SAXS curves of the IrO_2-HT sample were fitted with two different models that provide complementary information: a simple linear fit and the generalized Debye-Anderson-Brumberger (gDAB) model.[9,10]

The first approach is relevant to those materials displaying a SAXS curve in which the scattering cross section per area is proportional to a power law of the module of the scattering vector:

$$\left(\frac{1}{A}\frac{d\sigma}{d\Omega}\right)^{NP-IrOx} \propto q^{-\alpha} \quad [S7]$$

whereby the corresponding log vs. log plot displays a straight line with slope – α that is defined as follows:

$$\alpha = 6 - D_S \quad [S8]$$

where D_s is the surface fractal coefficient, whose value is limited to the range $2 \leq D_s \leq 3$. More precisely, when $D_s = 2$ the surface of the scattering object is smooth, whereas it is completely rough when $D_s = 3$.[11]

Complementarily, the gDAB model describes the scattering behavior of a two-phase system, which in this case would be constituted by the iridium oxide particles and the voids among them. The latter are in terms characterized by an undetermined shape and random distribution within the sample,[9] as unveiled by the HR-TEM images of the IrO_2-HT catalyst displayed in Fig. S11. The gDAB model mathematically describes the cross section per area as follows:

$$\left(\frac{1}{A}\frac{d\sigma}{d\Omega}\right)^{NP-IrOx} = \frac{\left(\Delta|f_{Ir}|^2 4\pi(1+2H)\right)^2}{\left[1+(q\xi)^2\right]^{\frac{3}{2}+H}} \qquad [S9]$$

where ξ is the correlation length and $\Delta|f_{Ir}|^2$ is the scattering contrast of iridium (for more details refer to the section below). Moreover, the Hurst exponent (H) was estimated following the same iterative procedure described above to determine D_f and β, and the resulting values was 0.5, thus indicating that the void in this catalyst is randomly distributed.[10] In fact, physically meaningful values of H should be limited to the range between 0 and 1, with the three sub-cases $0 \leq H < 0.5$, $H = 0.5$ and $0.5 < H \leq 1$ representing a space-filling Euclidean, a random distribution or a smooth Euclidean field, respectively.[10,12] In the gDAB model the correlation length corresponds to the pore average size and the fit led to a value of 2.32 ± 0.04 nm.[10]

Scattering contrast calculation procedure.– The scattering contrast $\Delta|f_{Ir}|^2$ is defined with the following Equation:

$$\Delta|f_{Ir}|^2 = |f_{Ir}(E_1)|^2 - |f_{Ir}(E_2)|^2 \qquad [S10]$$

where $f_{Ir}(E_1)$ and $f_{Ir}(E_2)$ are the atomic form factor of Ir at the X-ray energies of 11.160 and 11.210 keV (E_1 vs. E_2, respectively) use in the *in situ* SAXS measurements. The atomic form factor is a complex number and is a function of the X-ray photon energy irradiating the sample:

$$f_{Ir}(E) = Z + f'(E) + i \cdot f''(E) \qquad [S11]$$

where Z is the atomic number of the chemical element and, added to $f'(E)$, constitutes the real part of $f_{Pt}(E)$, while $f''(E)$ is the imaginary part. The values of $f'(E)$ and $f''(E)$ for each chemical element are reported in the Hephaestus database,[13] and lead to a calculated $\Delta|f_{Ir}|^2$ value of 605.91.

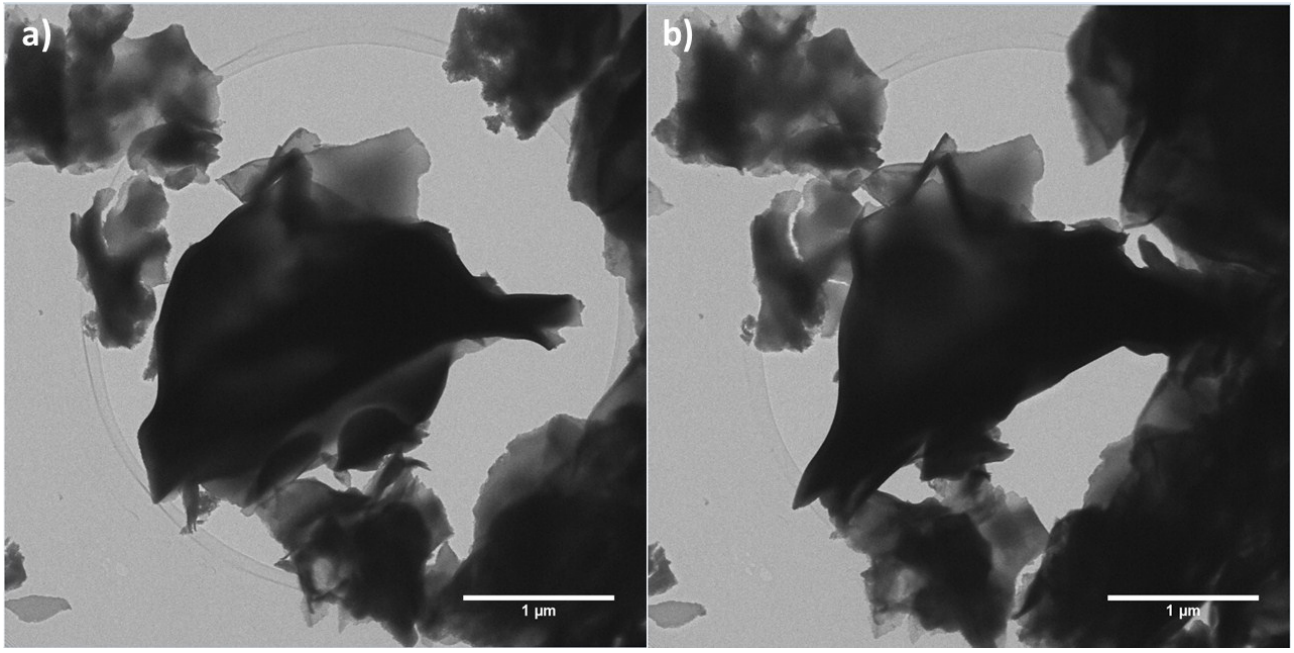

Fig. S16 Tomographic TEM images of the as-prepared IrO_x-AS catalyst acquired from two different angles

Statistical information implied in the data analysis

Log normal distribution.− The lognormal distribution (LN)[14] is a continuous distribution of a variable (in the case under analysis, the particle dimeter, *D*) characterized by a location parameter μ and a width parameter σ:

$$LN(D,\mu,\sigma) = \frac{1}{\sqrt{2\pi}D} exp\left(-\frac{ln(D/\mu)^2}{2\sigma^2}\right) \quad [S12]$$

The lognormal distribution is asymmetric and the average value <D> , the median (D_{median}) and the variance (Var(D)) are defined as follows:

$$< D >= \mu \cdot exp\left(\frac{\sigma^2}{2}\right) \quad [S13]$$

$$D_{median} = \mu \quad [S14]$$

$$Var(D) = \mu^2 \cdot exp(\sigma^2) \cdot \left(exp(\sigma^2) - 1\right) \quad [S15]$$

Pearson's second coefficient- Since the lognormal distribution is asymmetric it is possible to define its skewness, which represents the level of asymmetry of the distribution with respect to its average value. One statistical parameter representative of this skewness is Pearson's second coefficient (Sk_2), defined in the following Equation:[15]

$$Sk_2 = 3 \cdot \frac{D_{mean} - D_{median}}{SD} \quad [S16]$$

where SD is the standard deviation that is the square root of Var(D).

$$Sk_2 = 3 \cdot \frac{\mu \cdot exp\left(\frac{\sigma^2}{2}\right) - \mu}{\sqrt{Var(D)}} = 3 \cdot \frac{\left(exp\left(\frac{\sigma^2}{2}\right) - 1\right)}{exp\left(\frac{\sigma^2}{2}\right)\sqrt{exp(\sigma^2) - 1}} \quad [S17]$$

The evolution of these statistical parameters (i.e., Sk_2 and the width parameter σ) associated to the fitting of the SAXS curves acquired in the course of the electrochemical AST is displayed in below Figure S17. The fact that both variables decrease upon cycling implies that the lognormal distribution becomes narrower and more symmetric with respect to the mean value.

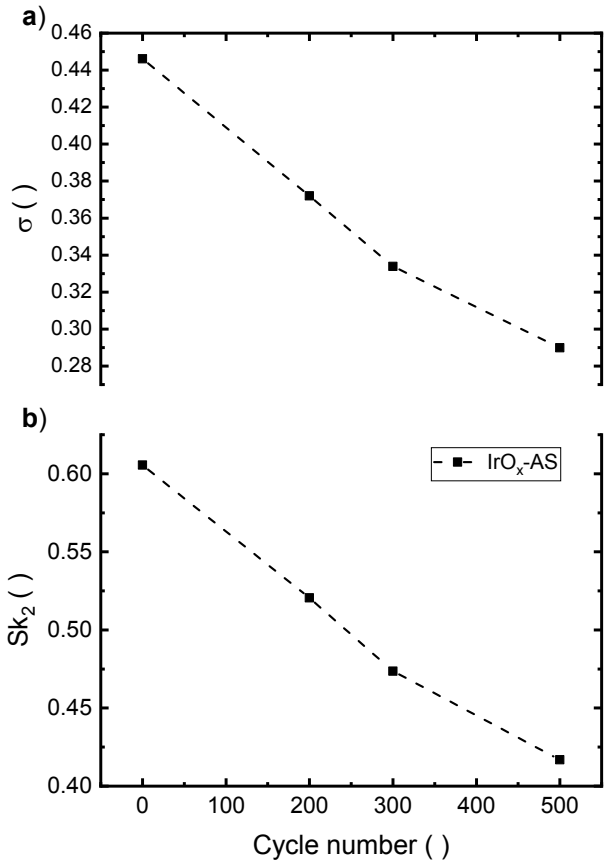

Fig. S17 Cycle-dependent evolution of the log normal distribution's width parameter (σ, a) and Pearson's second coefficient (Sk_2, b) derived from the fitting of the *in situ* SAXS results acquired in the course of the AST.

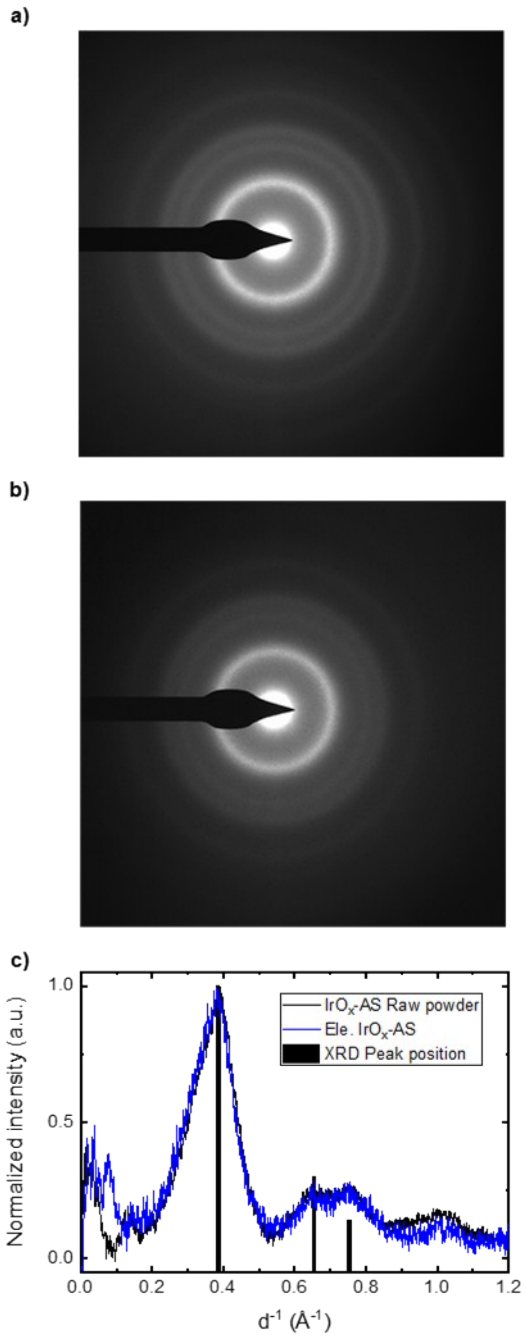

Fig. S18 Selected area electron diffraction patterns (collected over an area of 200 x 200 nm^2) of the as prepared IrO_x-AS sample (a) and a part of the post-mortem electrode of the same catalyst at the end of the electrochemical AST (b). Corresponding integrated profiles (c), whereby the black bars indicate the positions of the diffraction peaks observed in the XRD patter of the as-prepared catalyst in Figure 1c.

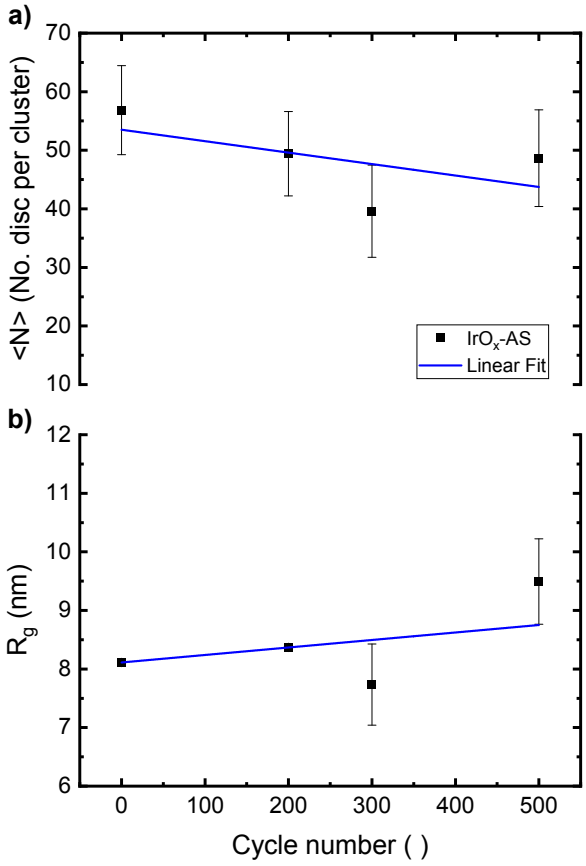

Fig. S19 Cycle-dependent evolution of the average number of particles per cluster (<N>, a) and of the cluster gyration radius (R_g, b) derived from the fitting of the *in situ* SAXS profiles acquired at 1.0 V vs. RHE for the IrO_x-AS catalyst.

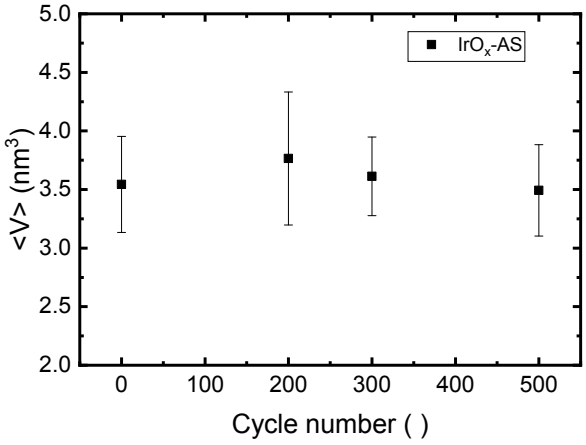

Fig. S20 Average disk volume (<V>) estimated using Eq. 7 (cf. manuscript), on the basis of the *in-situ* SAXS data acquired for the IrO_x-AS sample in the course of the electrochemical AST.

Estimated surface area (SA) of an IrO_2 monolayer

To verify that the SA values estimated on the basis of the A-SAXS results are do not exceed the maximum values that one could possibly expect for such iridium oxide materials, we calculated the theoretical maximum SA of a monolayer of Ir and O atoms. Such calculations were performed assuming that the Ir atoms are placed along rutile-like (101), (001) or (100) crystallographic planes, as represented in Fig. S21. Each (001) and (100) unit cell contains one atom of iridium, whereas two Ir atoms are held in each (101) unit cell. The SAs can then be estimated as the quotient between the plane surface (S) and its mass (m)

$$SA = \frac{S}{m} = \frac{2 \cdot A_{cell} \cdot A_N \cdot n_{mol}}{M_w \cdot n_{mol}} = \frac{2 \cdot A_{cell} \cdot A_N}{M_w} \qquad [S20]$$

where n_{mol} is the number of moles of IrO_2, A_N is the Avogadro number, and A_{cell} and M_w are the unit cell area and molar weight, respectively. All of these values and the corresponding SAs for each crystallographic orientation are reported in Table S9.

Table S9. Estimated surface areas (SAs) of IrO_2 monolayers with their atoms arranged in (101), (001) or (100) crystallographic orientations of the IrO_2 rutile-type (space group $P4_2/mnm$, $\alpha = \beta = \gamma = 90°$, $a = b = 4.5051$ Å, $c = 3.1586$ Å).[16]

Miller Index	A_{cell} (Å^2)	Stoichiometry	M_w (g·mol^{-1})	SA (m^2·g^{-1})
(101)	$(a^2+c^2)^{0.5} \cdot b = 24.7873$	Ir_2O_4	448.434	665.74
(001)	$a \cdot b = 14.2298$	IrO_2	224.217	764.36
(100)	$b \cdot c = 20.2959$	IrO_2	224.217	1090.21

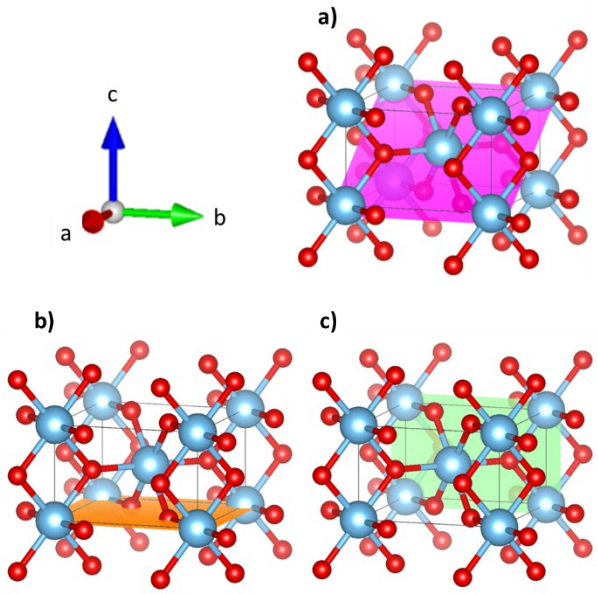

Fig. S21 Crystal structure of rutile-type IrO_2, whereby the differently colored planes in each panel represent the crystallographic planes (101) (a), (001) (b) or (100) (c). Note that the blue spheres correspond to Ir atoms and the red ones to O atoms.

References

1 D. F. Abbott, D. Lebedev, K. Waltar, M. Povia, M. Nachtegaal, E. Fabbri, C. Copérete and T. J. Schmidt, *Chem. Mater.*, 2016, **28**, 6591–6604.

2 C. D. Wagner, W. M. Riggs, L. E. Davis, J. F. Moulder and G. E. Muilenber, *Handbook of X-ray photoelectron spectroscopy*, Perkin-Elmer Corporation, Eden Prairie, 1978.

3 D. A. Shirley, *Phys. Rev. B*, 1972, **5**, 4709–4714.

4 J. H. Scofield, *J. Electron Spectros. Relat. Phenomena*, 1976, **8**, 129–137.

5 B. Ravel, The Artemis Users' Guide, http://bruceravel.github.io/demeter/artug/fit/happiness.html, (accessed March 21, 2019).

6 M. Povia, J. Herranz, T. Binninger, M. Nachtegaal, A. Diaz, J. Kohlbrecher, D. F. Abbott, B. J. Kim and T. J. Schmidt, *ACS Catal.*, 2018, **8**, 7000–7015.

7 C. M. Sorensen and G. M. Wang, *Phys. Rev. E*, 1999, **60**, 7143–7148.

8 T. Nicolai and D. Durand, *Phys. Rev. B*, 1994, **50**, 16357–16363.

9 P. Debye, H. R. Anderson and H. Brumberger, *J. Appl. Phys.*, 1957, **28**, 679–683.

10 R. Andersson, L. F. Van Heijkamp, I. M. De Schepper and W. G. Bouwman, *J. Appl. Crystallogr.*, 2008, **41**, 868–885.

11 D. W. Schaefer and K. D. Keefer, *Phys. Rev. Lett.*, 1986, **56**, 2199–2202.

12 B. B. Mandelbrot and J. R. Wallis, *Water Resour. Res.*, 1969, **5**, 321–340.

13 B. Ravel and M. Newville, *J. Synchrotron Radiat.*, 2005, **12**, 537–541.

14 E. Limpert, W. a. Stahel and M. Abbt, *Bioscience*, 2001, **51**, 341.

15 D. P. Doane and L. E. Seward, *J. Stat. Educ.*, 2011, **19**, DOI:10.1080/10691898.2011.11889611.

16 A. A. Bolzan, C. Fong, B. J. Kennedy and C. J. Howard, *Acta Crystallogr. Sect. B Struct. Sci.*, 1997, **53**, 373–380.